A UNIFIED SOURCE MODEL
FOR THE 1906 SAN FRANCISCO EARTHQUAKE

Seok-Goo Song, Gregory C. Beroza, Paul Segall

Abstract

We reconcile two previously discordant source models of the 1906 San Francisco earthquake and obtain a model that satisfies both triangulation and seismic data by allowing the rupture velocity to exceed the shear wave velocity. Employing a projection method to remove the dependence on initial station positions allowed us to make use of a more stable triangulation network, including non-repeated angle observations along the northern San Andreas fault. This strengthens the case for significant slip over the entire northern segment of the San Andreas fault from San Juan Bautista to Cape Mendocino during the 1906 earthquake. We also found that the teleseismic body wave data can be reconciled with the geodetically derived slip model by allowing super-shear rupture. This resolves a longstanding conflict between the two previous slip models (geodetic and seismic) of this earthquake. Super-shear rupture has long been recognized as a theoretical possibility for strike-slip faulting, and it has been observed in several recent large strike-slip earthquakes, which raises the prospect that it might be typical for such events. Super-shear rupture leads to substantially different strong ground motion and as a result, may need to be taken into account when developing ground motion prediction relations for large strike-slip earthquakes. Our final slip model has a seismic moment of 7.9×10^{20} N-m, which corresponds to a moment magnitude of Mw 7.9

Introduction

The 1906 San Francisco earthquake ruptured the northern segment of the San Andreas fault at the dawn of the twentieth century and is perhaps the single most important earthquake in the history of earthquake science. Despite the importance of the earthquake, the two most recently published source models, one based on geodetic data (Thatcher *et al*., 1997) and the other based on seismic data (Wald *et al*., 1993), differ substantially from one another, particularly in the total rupture length. The geodetic slip model maps slip from San Juan Bautista to Cape Mendocino (~500 km rupture length); whereas, the seismic model finds almost no slip north of Point Arena (~300 km rupture length). We find that these two models can be reconciled if the rupture velocity exceeded the shear wave velocity of the Earth's crust north of San Francisco.

While it is often assumed that earthquake rupture velocity does not exceed the Rayleigh wave velocity, theoretical studies indicate that in-plane rupture can propagate at inter-sonic speeds; i.e., between the *S*-wave and the *P*-wave velocities (Burridge, 1973; Andrews, 1976). Recent large strike-slip earthquakes: the 1999 Izmit, Turkey; the 2001 Kunlunshan, Tibet; and the 2002 Denali events, have all exhibited characteristics of super-shear rupture (Bouchon *et al*., 2001; Bouchon and Vallée, 2003; Dunham and Archuleta, 2004; Ellsworth *et al*., 2004). Recent laboratory experiments (Rosakis *et al*., 1999; Xia *et al*., 2004) confirm and extend previous theoretical work on super-shear rupture propagation. Thus it seems plausible that super-shear rupture could have occurred during the 1906 San Francisco earthquake.

Geodetic Analysis

The differences between existing source models are primarily north of Point Arena, where the San Andreas fault runs offshore, rendering direct observation of surface rupture impossible. 4.9 meters of slip was measured at Alder Creek, the northernmost observation of unambiguous faulting in the 1906 earthquake (Lawson, 1908). The same report found offset at Seal Cove, farther to the north, where the fault comes on shore again, but raised the possibility that this offset might have been due to landslides rather than tectonic faulting.

Only repeated triangulation observations were used to estimate slip in the previous geodetic study (Thatcher *et al*., 1997), resulting in a weakly connected network especially north of Point Arena and hence large uncertainties in the inferred displacements. In this study we utilize all of the available triangulation measurements in the northern region, employing a projection method to remove the dependence on initial station positions (Yu and Segall, 1996). This allows us to strengthen this part of the network using non-repeated observations (Fig. 1). It can be shown that the Yu and Segall (1996) method reduces to the standard approach, using only repeated angle measurements, when all of the measurements are repeated before and after the earthquake (Appendix). Our data set in this region contains 60 pre-1906 and 172 post-1906 angle observations, respectively, compared with the 37 angle changes used in the previous study. We used the same data set, consisting of repeated angles, in the southern region (see Figure 2).

The geodetic displacements along the entire rupture trace of the 1906 earthquake were estimated (Fig. 2 and 3, Table 1 in E) using a model coordinate solution (Segall and Matthews, 1988) to constrain rigid body motions and scale changes. The result shows a displacement field characteristic of the co-seismic faulting as far north as Cape Mendocino (Fig. 2. (a)). Two stations near the fault trace immediately south of Cape Mendocino show large displacements parallel to the changing local strike of the fault, which strongly supports fault slip as opposed to land-sliding in this area. The magnitude of these displacement vectors indicates that the amount of fault slip that caused them is substantial.

We estimate the co-seismic slip distribution by a linear inversion of the triangulation data (Fig. 4 and Table 2 in E) using the surface trace from the new 3-D geologic model constructed by Jachens *et al*. (2006). A homogeneous elastic half-space was assumed in the forward calculation. An appropriate level of smoothing was determined by cross validation (Matthews and Segall, 1993) and used in the inversion. The idea behind cross validation is that a good model should predict data not used in the estimation. The appropriate smoothing is determined by testing what level of smoothing generates a model that best predicts the unused data. In our model slip varies only in the horizontal direction along the fault trace as shown in figure 2. Each value along the fault indicates averaged slip on a 10 km long and 12 km wide (deep) vertical fault patch. The fault is assumed to be extended vertically with 90° dip. We note that the average slip on each patch trades off with the assumed vertical extent of the fault (12 km in this study), with the result that, for example, models with greater depth extent but smaller averaged slip can fit the data equally well. But the integral of slip in the vertical direction should not change much irrespective of the assumed rupture width within a reasonable range of the seismogenic zone in California. Due to our inability to obtain the original data records, the slip distribution south of Point Arena is constrained only by the same repeated angle observations used in the previous study (Thatcher *et al*., 1997). The slip north of Point Arena is significantly improved by the use of non-repeated angle measurements. Our slip on a ~500 km long rupture successfully fits the triangulation data, both confirming and refining the previous geodetic analysis (Thatcher *et al*., 1997).

Seismic Analysis

With the mapped surface slip and geodetic data both consistent with the longer fault rupture, the short rupture length inferred from the seismic data stands out. For long strike slip events like the 1906 San Francisco earthquake, the duration of observed waveforms is related to the ratio of rupture length to rupture velocity; however, the duration of the observed teleseismic waves and the fixed 2.7 km/sec sub-Rayleigh rupture velocity assumed previously (Wald *et al*., 1993), favors a shorter fault rupture. Our hypothesis is that by allowing more flexibility in the rupture velocity, including the potential for super-shear rupture, we might fit all data with a single model.

The 1906 earthquake was recorded by over 90 seismographic stations worldwide and both seismograms and background information are well preserved (Reid, 1910). However, the data quality reflects the fact that these were the early days of instrumental seismology. Most stations are not useful for waveform inversion. We used 5 stations, 8 components in total; two Wiechert

Pendulum records from Europe (Uppsala, Sweden and Gottingen, Germany), two Omori records from Japan (Kobe and Osaka), and one Bosch-Omori record from the Caribbean (Puerto Rico). Two Omori stations in Japan have only one component. Those 5 stations were selected based on the proximity of observed Green's functions to the 1906 records and the need for spatial/azimuthal coverage. Detailed information on the seismic data is well documented by the previous study (Wald *et al*., 1993).

We apply a Bayesian inversion approach coupled with a Monte Carlo sampling method (the Metropolis algorithm) (Mosegaard and Tarantola, 2002; Metropolis *et al*., 1953). The posterior distribution of the model (slip and rupture velocity) is proportional to the product of a prior distribution and a likelihood function. The likelihood function contains only the seismic data and the geodetic inversion results obtained above were used in the prior distribution in order to stabilize the slip in the inversion, which we believe was relatively well resolved in the linear geodetic inversion. The prior for the rupture velocity is a Gaussian distribution centered at the previously used sub-Rayleigh velocity (2.7 km/sec) with a 0.5 km/sec standard deviation. By assuming sub-shear rupture velocity in the prior, we ensure that the method will only find super-shear rupture if the data require it.

We use waveforms from the 1984 M 6.2 Morgan Hill earthquake as empirical Green's functions to calculate teleseismic waveforms (Wald *et al*., 1993). Both the Morgan Hill and the 1906 San Francisco earthquake are vertical strike-slip events and share approximately the same strike (~ N35°W), in particular, in the central portion of the 1906 rupture. But the San Andreas fault bends in the northern and southern portion of the study area as shown in Figure 2. The average strike of these segments is about 10 ~ 15° different from that of the Morgan Hill earthquake, such that modest error is introduced by using the same Green's function for the entire fault trace. The

Green’s function is time-lagged with elapsed rupture time along the fault trace from the hypocenter and a linear summation of the time-lagged Green’s function weighted by slip provides synthetic waveforms for the 1906 earthquake. We did not explicitly consider the detailed shape of temporal evolution of slip and rise time in the inversion because that is well beyond the resolving power of the data.

As discussed in detail by Wald *et al*. (1993), the age and quality of the seismic data limit the resolution of source characteristics for the 1906 earthquake. The uncertain instrument response, limited accuracy of the available Green’s functions, particularly when applied to the northernmost end of the fault, and complex wave propagation effects for the SV component, all contribute to the data residuals. A waveform inversion without the analysis of very long period data (>40 sec) may underestimate the rupture area of large earthquakes as observed in the Sumatra earthquake (Stein and Okal, 2005). Despite the limited data coverage quality, forward modeling indicates that the duration and amplitude of the teleseismic waves can constrain the overall duration of the rupture, and hence the average rupture velocity when combined with the fault length determined from the geodetic data.

Super-shear Rupture and Combined Slip Model

Sensitivity tests indicate that, because of the geometry of the problem, rupture north of the hypocenter is primarily constrained by the two European seismograms (Gottingen and Uppsala) while rupture to the south is primarily constrained by the Puerto Rico data. Thus, we first tried a two-segment rupture velocity model split at the hypocenter and solved for a single rupture velocity on each of these two segments. Several locations have been suggested for the hypocenter of the earthquake by analyzing local and teleseismic observations (Reid, 1910; Bolt, 1968; Lomax, 2005). We used the latest estimate determined by A. Lomax (2005), which is located about 3 km west of the San Francisco zoo. We find that it takes about 85 and 52 seconds, respectively, for the rupture to propagate along the northern (330 km long) and southern (150 km) segment from the hypocenter, which indicates that the rupture travels to the north at an average speed of 3.9 +/- 0.1 km/sec, exceeding the average shear wave velocity of the Earth's crust north of San Francisco, and to the south at 2.9 +/- 0.1 km/sec, respectively. The standard errors of the rupture velocity estimates are quite small, due to the fact that neighboring points in seismic waveforms are highly correlated, a fact not accounted for in the inversion. In an attempt to localize the rupture velocity, we divided the rupture into five segments (3 segments north of the hypocenter, 110 km for each; 2 segments to the south, 70 and 80 km for each). While it is possible that the data could resolve such spatial variations in rupture velocity, the fact that the total rupture durations north and south of the hypocenter are about the same in both the two and five segment models (Fig. 5) suggests that while super-shear rupture to the north of the hypocenter is required to fit the data, it may be difficult to localize it further.

Figures 6 and 7 show the slip and waveform comparisons, respectively, obtained from the two segment model. A digitized version of the slip estimates are given in Table 2 (E). The slip in the northern segment is smoother than that obtained solely from geodetic data (Fig. 4), but there is significant slip in the northern region of the fault. This confirms that the long rupture length (~500 km) is compatible with the seismic data, although the amount of slip is somewhat smaller than the geodetically preferred value. The synthesized waveform envelopes capture the duration and amplitude of the seismograms and reasonable waveform fits are achieved at the European stations even though the objective function is defined using the waveform envelopes (Fig. 7). The polarity of the synthetic waveform (SV component) at the PTR station is reversed. This can occur while fitting the waveform envelope because it does not preserve polarity information. Inaccurate arrival time alignment, an inaccurate Green's function, reversed polarity on the instrument, and delayed rupture propagation to the southeast are all possible explanations of this mismatch.

Because the fit at PTR is primarily controlled by the slip and rupture propagation to the southeast of the hypocenter, it does not affect the inference that the rupture extended a total length of 500 km nor that rupture to the north of the hypocenter was super-shear.

Our final slip model has an average slip of 4.3 meters and a seismic moment of 7.9×10^{20} N-m, which corresponds to a moment magnitude of Mw 7.9. Although the final slip model was obtained by a joint inversion of the geodetic and seismic data, the final static slip distribution is primarily constrained by the triangulation data. Because the triangulation survey data used in this study span an interval as long as 40 years, our slip estimates include postseismic and interseismic, as well as coseismic deformation. Because the long-term aseismic strain accumulates in the opposite direction of the deformation caused by earthquakes, i.e. right-lateral strain accumulation between earthquakes vs. right-lateral strain release during the earthquake, our estimate of Mw 7.9 should be considered a lower bound on the size of the 1906 earthquake in that sense. However afterslip at seismogenic depths, which is very difficult to constrain given the data available, could bias the estimated magnitude to higher values.

Discussion and Implications

The long rupture length is also strongly supported by seismic intensity data from the 1906 earthquake (Boatwright and Bundock, 2005). The intensity map clearly shows the severely damaged area (intensity VII or larger) extending north to the Mendocino triple junction and rules out the possibility that the slip on the fault north of Point Arena occurred aseismically. Moreover, a recent examination of the northernmost San Andreas fault near Shelter Cove concluded that slip mapped there in 1906 was likely tectonic, extensive, and located on the main trace of the San Andreas fault (Prentice *et al.*, 1999).

A simpler analysis of the waveform data that does not directly model the spatial variation of slip also supports super-shear rupture north of the hypocenter (Fig. 8). Deconvolution of the empirical Green's functions from the 1906 seismograms yields an estimate of the apparent source duration and, given the fault length, the average rupture velocity. Using the European stations and employing positivity, smoothness, and moment-minimization constraints in a time domain deconvolution of the empirical Green’s function event from the 1906 mainshock, we find a duration of ~ 75 seconds, which corresponds to an average rupture velocity of ~3.4 km/sec north of the hypocenter. This should be regarded as a lower bound since the smoothness constraint on the source time function deconvolution results in a longer duration, and hence lower inferred rupture velocity.

Both the intensity data and the deconvolution support our long rupture length slip model with super-shear rupture. If the rupture velocity in this earthquake were super-shear, as we have suggested, then it has important implications for seismic hazard. First it demonstrates that slip models derived from geodetic and seismic observations are compatible, which is relevant for northern California because it provides a unified slip model to be used in recurrence models for future earthquakes. More generally, because the nature of strong ground motion for earthquakes that undergo super-shear rupture is profoundly different from those where the rupture is sub-shear (Aagaard and Heaton, 2004), it will be necessary to account for this when predicting both the level and the variability of strong ground motion in future large strike-slip earthquakes.

Acknowledgments

We thank David Wald for providing us with his digitized teleseismic data and Wayne Thatcher for sharing his notes on the triangulation data. We also thank the National Geodetic Survey for helping us extract triangulation data from their archives. We greatly benefited from the advice, criticism, and assistance of David Wald, Jack Boatwright, and Brad Aagaard throughout the study and thank two reviewers, David Wald and Pengcheng Liu, for their insightful comments, which improved the manuscript. This research was supported by the U.S. Geological Survey (USGS), Department of Interior, under USGS award number 06HQGR0025. The views and conclusions contained in this document are those of the authors and should not be interpreted as necessarily representing the official policies, either expressed or implied, of the U. S. Government.

References

Aagaard, B. T., and T. H. Heaton (2004). Near-source ground motions from simulations of sustained intersonic and supersonic fault ruptures, *Bull. Seism. Soc. Am.* **94**, 2064-2078.

Andrews, D. J. (1976). Rupture velocity of plane strain shear cracks, *J. Geophys. Res.* **81**, 5679-5687.

Boatwright, J., and H. Bundock (2005). Modified Mercalli Intensity maps for the 1906 San Francisco earthquake plotted in shake-map format, *U. S. Geol. Surv. Open-File Rept.* 2005-1135.

Bolt, B. A. (1968). The focus of the 1906 California earthquake, *Bull. Seism. Soc. Am.* **58**, 457-471.

Bouchon, M., M. P. Bouin, H. Karabulut, M. N. Toksöz, M. Dietrich, and A. Rosakis (2001). How fast is rupture during an earthquake? New insights from the 1999 Turkey earthquakes, *Geophys. Res. Lett.* **28**, 2723-2726.

Bouchon, M., and M. Vallée (2003). Observation of long supershear rupture during the magnitude 8.1 Kunlunshan earthquake, *Science* **301**, 824-826.

Burridge, R. (1973). Admissible speeds for plane-strain shear cracks with friction but lacking cohesion, *Geophys. J. R. Astr. Soc.* **35**, 439-455.

Dunham, E. M., and R. J. Archuleta (2004). Evidence for a supershear transient during the 2002 Denali fault earthquake, *Bull. Seism. Soc. Am.* **94**, S256-S268.

Ellsworth, W.L., M. Celebi, J.R. Evans, E.G. Jensen, R. Kayen, M.C. Metz, D.J. Nyman, J.W. Roddick, P. Spudich, C.D. Stephens (2004). Near-field ground motion of the 2002 Denali fault, Alaska, earthquake recorded at Pump Station 10, *Earthquake Spectra*, **20**, 597-615.

Jachens, R., R. Simpson, R. Graymer, C. Wentworth, and T. Brocher (2006). Three-dimensional geologic map of northern and central California: A basic model for supporting earthquake simulations and other predictive modeling, *Seism. Res. Lett.* **77**, 270-271.

Lawson, A. C. (1908). The California earthquake of April 18, 1906, Report of the State Earthquake Investigation Commission, Vol. 1, A. C. Lawson, Chairman, Carnegie Inst. of Washington, Washington, D. C. (reprinted 1969).

Lomax, A. (2005). A reanalysis of the hypocentral location and related observations for the great 1906 California earthquake, *Bull. Seism. Soc. Am.* **95**, 861-877.

Matthews, M. V., and P. Segall (1993). Statistical inversion of crustal deformation data and estimation of the depth distribution of slip in the 1906 earthquake, *J. Geophys. Res.* **98**, 12,153-12,163.

Metropolis, N., A. W. Rosenbluth, M. N. Rosenbluth, A. H. Teller, and E. Teller (1953). Equation of state calculations by fast computing machines, *J. Chem. Phys.* **21**, 1087-1092.

Mosegaard, K, and A. Tarantola (2002). Probabilistic approach to inverse problems, in *International Handbook of Earthquake & Engineering Seismology*, Part A., edited by W. H. K. Lee *et al*., pp. 237-265, Academic Press, San Diego, California.

Prentice C. S., D. J. Merritts, E. C. Beutner, P. Bodin, A. Schill, and J. R. Muller (1999). Northern San Andreas fault near Shelter Cove, California, *Geol. Soc. Am. Bull.* **111**, 512-523.

Reid, H. F. (1910). *The mechanics of the earthquake*, The California earthquake of April 18, 1906, Report of the State Earthquake Investigation Commission, Vol. 2, A. C. Lawson, Chairman, Carnegie Inst. of Washington, Washington, D. C. (reprinted 1969).

Rosakis, A. J., O. Samudrala, and D. Coker (1999). Cracks faster than the shear wave speed, *Science* **284**, 1337-1340.

Segall, P., and M.V. Matthews (1988). Displacement calculations from geodetic data and the testing of geophysical deformation models, *J. Geophys. Res.* **93**, 14,954-14,966.

Stein, S., and E. A. Okal (2005). Speed and size of the Sumatra earthquake, *Nature* **434**, 581 – 582.

Thatcher, W., G. Marshall, and M. Lisowski (1997). Resolution of fault slip along the 470-km-long rupture of the great 1906 San Francisco earthquake and its implications, *J. Geophys. Res.* **102**, 5353-5367.

Wald, D. J., H. Kanamori, D. V. Helmberger, and T. H. Heaton (1993). Source study of the 1906 San Francisco earthquake, *Bull. Seism. Soc. Am.* **83**, 981-1019.

Xia, K., A. J. Rosakis, and H. Kanamori (2004). Laboratory earthquakes:the sub-Rayleigh-to-supershear transition, *Science* **303**, 1859-1861.

Yu, E., and P. Segall (1996). Slip in the 1868 Hayward earthquake from the analysis of historical triangulation data, *J. Geophys. Res.* **101**, 16,101-16,118.

Department of Geophysics

Stanford University

397 Panama Mall

Stanford, CA 94305-2215

(S.S.,P.S.,G.C.B.)

Figure Captions

Fig. 1. Triangulation network in the northern region of the San Andreas fault used in the inversion before (a) and after (b) the 1906 San Francisco earthquake compared with network (c) of repeated angles only (Thatcher *et al.*, 1997). The fault trace used in the study (Jachens *et al.*, 2006) is shown as a thick solid line in (a) and (b). The solid line in (c) shows a fault trace used in the previous study. The time spans of the triangulation surveys before and after the earthquake are 1878-1892 and 1925-1942, respectively. An average standard deviation in angle measurement errors is less than 1 arc-sec for the post 1906 data set and about two arc-seconds for the pre 1906 data.

Fig. 2. Estimated model coordinate displacement fields (blue arrows) with 95 % confidence ellipses in the northern (a) and southern (b) region of the 1906 rupture area. Predicted displacements from the estimated geodetic slip model and the San Andreas fault trace (Jachens *et al.*, 2006) in the region are shown as red arrows and thick solid line, respectively. Stations near the fault in the northern region (a) show large displacements parallel to the local fault strike.

Fig. 3. As for Figure 2, the estimated model coordinate displacement fields (blue arrows) with 95 % confidence ellipses in four local networks; (a) Point Arena, (b) Fort Ross, (c) Tomales Bay, (d) Colma.

Fig. 4. Slip model obtained from inversion of geodetic data only with 2 sigma errors. The two previous slip models are also given for comparison (Thatcher *et al.*, 1997; Wald *et al.*, 1993). Slip varies only in the horizontal direction and each value along the fault indicates averaged slip on each 10 km (length) by 12 km (width) fault patch. Slip in the northern region is primarily

constrained by two nearby stations, resulting in relatively large errors in this region. The larger errors notwithstanding, these results strongly support large slip in this region. Slip distribution in the southern region is very similar to the previously obtained geodetic model because we used the same data set in that region. We did, however, find large slip between Fort Ross and Tomales Bay, although it was smoothed in the previous geodetic model (Thatcher *et al*., 1997).

Fig. 5. Rupture time distribution along the fault with two segment (a) and five segment model (b). *P*- and *S*-wave propagation times are also provided from the average *P*- and *S*-wave speed along the San Andreas fault. Despite variations in the five segment model, the total rupture durations north and south of the hypocenter are about the same for the two and five segment model, about 85 seconds for the 330 km northern segment and about 52 seconds for the 150 km southern segment, respectively.

Fig. 6. Final slip models with 2 sigma errors obtained from both geodetic and seismic data compared with two previous slip models. Significant slip is observed in the northern region of the fault although the actual amount of slip is somewhat smaller than the previous geodetic slip (Thatcher *et al*., 1997). The rest is the same as Figure 4.

Fig. 7. Comparison of observed (solid) and calculated (dashed) waveforms and their envelopes. Data are direct S-phases band-pass filtered between 0.01 and 0.1 Hz. Maximum amplitudes are given on the left of each trace in mm at the WWSSN LP seismograph (top: observed, bottom: calculated). The calculated waveform envelopes successfully reproduce most of the amplitude and duration information of the observed waveform envelopes. Some stations also achieve good waveform fitting although our objective function is based on the waveform envelopes (GOT: Gottingen, Germany, UPP: Uppsala, Sweden, PTR: Puerto Rico, W.I., KOB: Kobe, Japan, OSK: Osaka, Japan).

Fig. 8. Total rupture duration of the earthquake inferred from the deconvolution of observed waveforms. (a) Apparent source time functions for two European stations (GOT and UPP), obtained from deconvolving the empirical Green's functions of the Morgan Hill earthquake from the observed waveforms. (b) Stacked version of the all source time functions except the SH component of the Uppsala station. (c) Expected duration of waveforms at each station as a function of the rupture velocity north of the hypocenter. The rupture velocity south of the hypocenter was fixed as 2.9 km/sec. The expected duration of waveforms were calculated from the maximum difference of arrival times from each fault patch. The duration of the apparent source time functions are well defined at each component except for the Uppsala SH, and is quite well resolved in the stacked source time function (b). The apparent rupture duration at the two European stations is about 75 seconds which is equivalent to a 3.4 km/sec average rupture velocity north of the hypocenter. This independent measure of the total rupture duration of the earthquake supports the high rupture velocity, although the estimated velocity is somewhat less than in the kinematic slip inversion.

Appendix

Here we show that the denuisancing procedure of Yu and Segall (1996) reduces to the standard method, using the differences between repeated angles, when the pre and post earthquake networks are identical. That is, when all angles are repeated. Yu and Segall (1996) write the equations relating angle measurements $\mathbf{d}\boldsymbol{\theta}$ to the coordinate corrections at the initial epoch $\mathbf{dx}_1$ and displacements $\mathbf{u}$ as

$$\begin{bmatrix} \mathbf{d}\boldsymbol{\theta}_1 \\ \mathbf{d}\boldsymbol{\theta}_2 \end{bmatrix} = \begin{bmatrix} A_1 \\ A_2 \end{bmatrix} \mathbf{dx}_1 + \begin{bmatrix} 0 \\ A_2 \end{bmatrix} \mathbf{u}, \tag{1}$$

where the subscripts 1 and 2 refer to the initial and final surveys. The displacements are assumed to arise from fault slip $\mathbf{s}$ in an elastic medium so that $\mathbf{u} = G\mathbf{s}$, and (1) become

$$\begin{bmatrix} \mathbf{d}\boldsymbol{\theta}_1 \\ \mathbf{d}\boldsymbol{\theta}_2 \end{bmatrix} = \begin{bmatrix} A_1 \\ A_2 \end{bmatrix} \mathbf{dx}_1 + \begin{bmatrix} 0 \\ A_2 G \end{bmatrix} \mathbf{s}. \tag{2}$$

If the network geometry is identical in both surveys then $A_1 = A_2 \equiv A$ and subtracting the first set of equations from the second leads directly to

$$\mathbf{d}\boldsymbol{\theta}_2 - \mathbf{d}\boldsymbol{\theta}_1 = AG\mathbf{s}. \tag{3}$$

In this case the changes in angles are directly related to the fault slip with no need to consider the corrections to the initial coordinates. For least squares estimation (3) lead to normal equations

$$G^T A^T (\mathbf{d}\boldsymbol{\theta}_2 - \mathbf{d}\boldsymbol{\theta}_1) = G^T A^T AG\mathbf{s}. \tag{4}$$

We now consider the denuisancing procedure. Equation (2) can be written more compactly as

$$\mathbf{d}\boldsymbol{\theta} = \Psi \mathbf{dx} + \Omega \mathbf{s}. \tag{5}$$

Yu and Segall (1996) define a projection operator Q that annihilates the dependence on $\mathbf{dx}$

$$Q \equiv I - \Psi \Psi^{\dagger} \tag{6}$$

where I is an identity matrix and $\Psi^{\dagger}$ is the generalized inverse of Ψ. Premultiplying (5) by Q leads to

$$Q\mathbf{d}\boldsymbol{\theta} = Q\Omega\mathbf{s}, \tag{7}$$

since

$$Q\Psi = (I - \Psi\Psi^{\dagger})\Psi = \mathbf{0}. \tag{8}$$

A least squares estimate of fault slip then follows from the normal equations

$$\Omega^T Q\mathbf{d}\boldsymbol{\theta} = \Omega^T Q\Omega\mathbf{s}, \tag{9}$$

since Q is both symmetric and idempotent.

If the network geometry is repeated then

$$\Psi = \begin{bmatrix} A \\ A \end{bmatrix}. \tag{10}$$

The matrix A has singular value decomposition (SVD) given by $A = U_p S_p V_p^T$, where p is the number of non-zero singular values. It follows then that Ψ has an SVD with the same singular vectors spanning the model space V and repeated data space singular vectors given by

$$\begin{bmatrix} \frac{1}{\sqrt{2}}U_p \\ \frac{1}{\sqrt{2}}U_p, \end{bmatrix}, \tag{11}$$

where the factor of $1/\sqrt{2}$ arises due to normalization. Thus, in this case the projection operator Q is

$$Q = \begin{bmatrix} I - \frac{1}{2}H & -\frac{1}{2}H \\ -\frac{1}{2}H & I - \frac{1}{2}H \end{bmatrix}, \tag{12}$$

where $H \equiv AA^{\dagger} = U_p U_p^T$. Substituting (12) into (9) leads to

$$\begin{aligned} G^T A^T[(I - \frac{1}{2}H)\mathbf{d}\boldsymbol{\theta}_2 - \frac{1}{2}H\mathbf{d}\boldsymbol{\theta}_1] &= G^T A^T (I - \frac{1}{2}H)AG\mathbf{s} \\ \frac{1}{2}G^T A^T(\mathbf{d}\boldsymbol{\theta}_2 - \mathbf{d}\boldsymbol{\theta}_1) &= \frac{1}{2}G^T A^T AG\mathbf{s}, \end{aligned} \tag{13}$$

since $A^T H = (HA)^T = (AA^{\dagger}A)^T = A^T$. Comparing (13) to (4) we see that both methods lead to the same result when all angles are repeated. The denuisancing procedure, however, allows all measurements to be used when the angles are not all repeated.

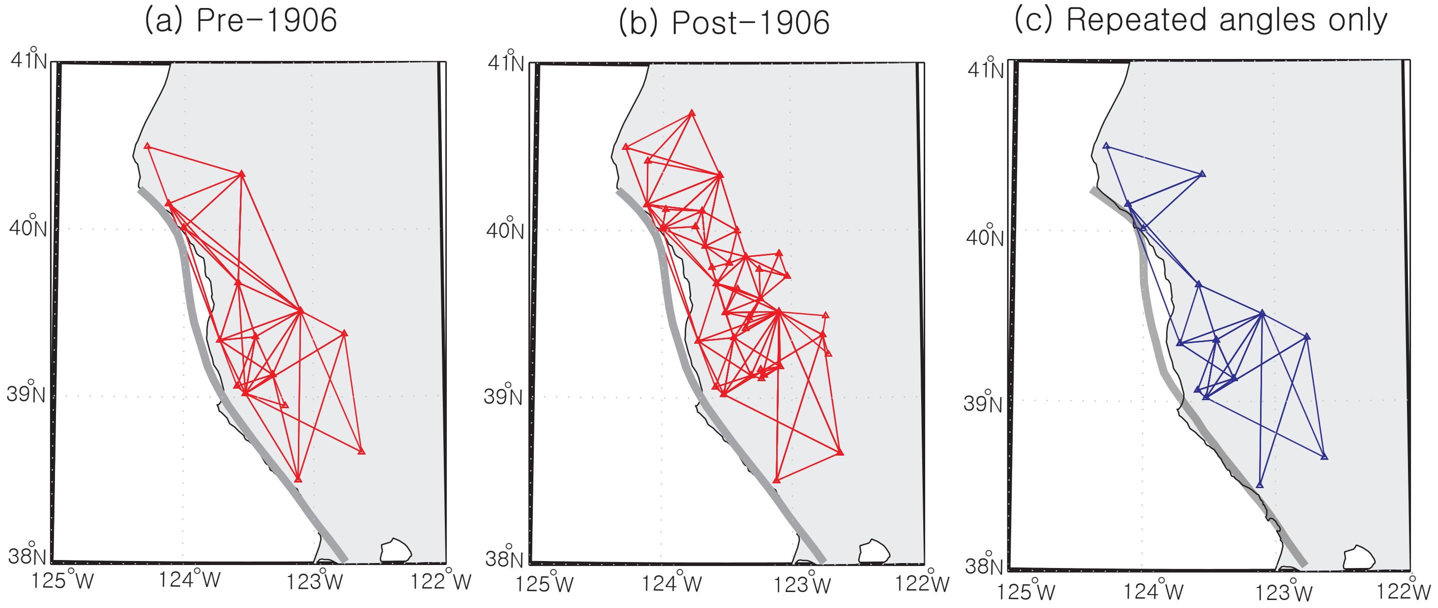

(a) Pre-1906

(b) Post-1906

(c) Repeated angles only

Figure 1

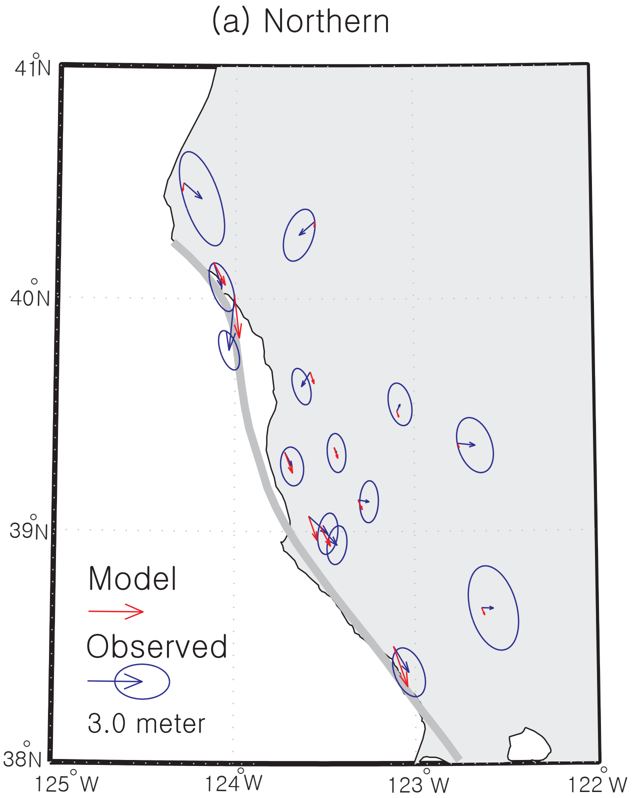
(a) Northern
(b) Southern
41°N
40°N
39°N
38°N
125°W
124°W
123°W
122°W
39°N
38°N
37°N
36°N
124°W
123°W
122°W
121°W
Model
Observed
3.0 meter
Model
Observed
3.0 meter

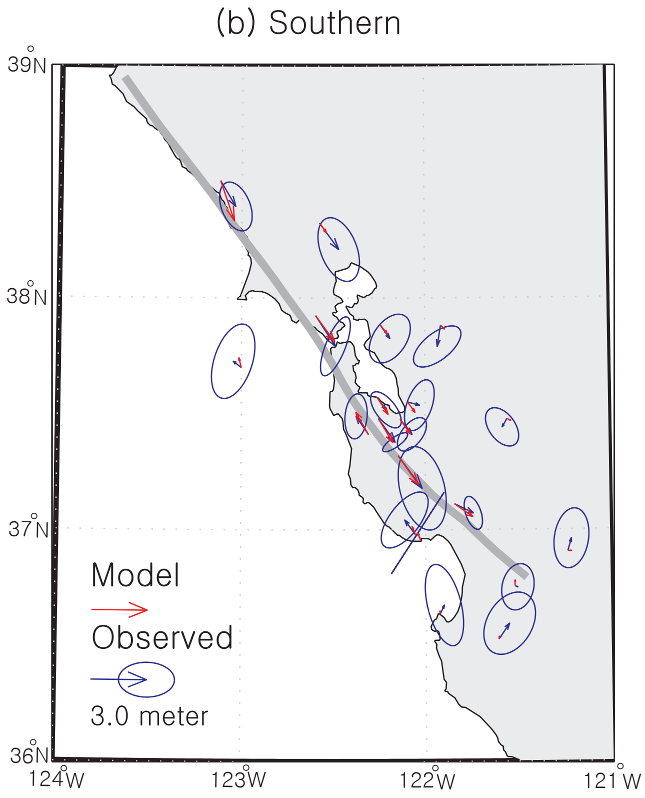

Figure 2

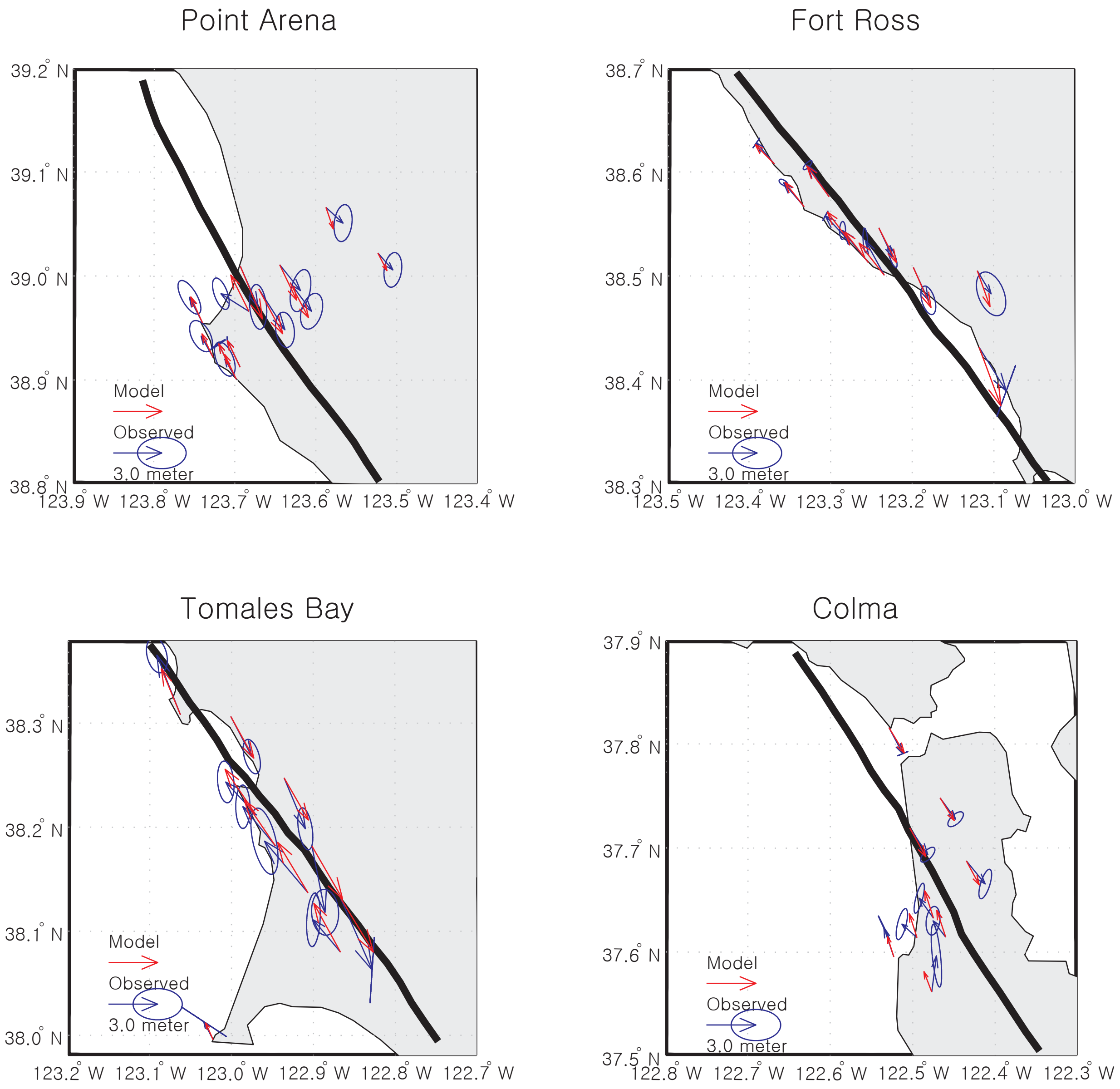
Point Arena
39.2° N
39.1° N
39.0° N
38.9° N
38.8° N
123.9° W
123.8° W
123.7° W
123.6° W
123.5° W
123.4° W
Model
Observed
3.0 meter
Fort Ross
38.7° N
38.6° N
38.5° N
38.4° N
38.3° N
123.5° W
123.4° W
123.3° W
123.2° W
123.1° W
123.0° W
Model
Observed
3.0 meter
Tomales Bay
38.3° N
38.2° N
38.1° N
38.0° N
123.2° W
123.1° W
123.0° W
122.9° W
122.8° W
122.7° W
Model
Observed
3.0 meter
Colma
37.9° N
37.8° N
37.7° N
37.6° N
37.5° N
122.8° W
122.7° W
122.6° W
122.5° W
122.4° W
122.3° W
Model
Observed
3.0 meter

Figure 3

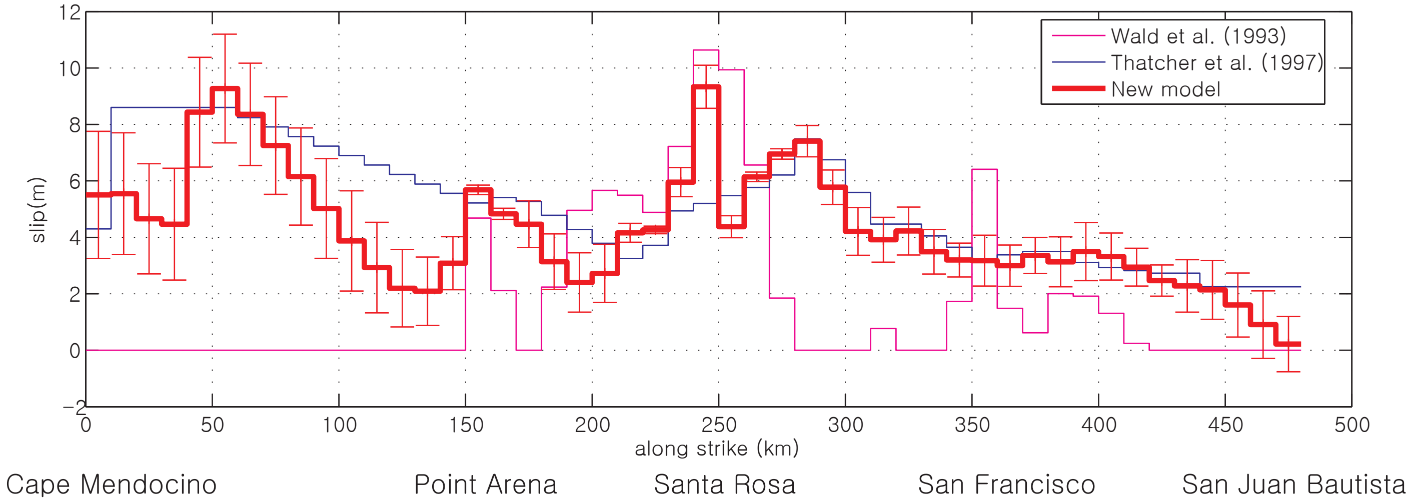

Wald et al. (1993)
Thatcher et al. (1997)
New model
slip(m)
12
10
8
6
4
2
0
−2
0
50
100
150
200
250
300
350
400
450
500
along strike (km)
Cape Mendocino
Point Arena
Santa Rosa
San Francisco
San Juan Bautista

Figure 4

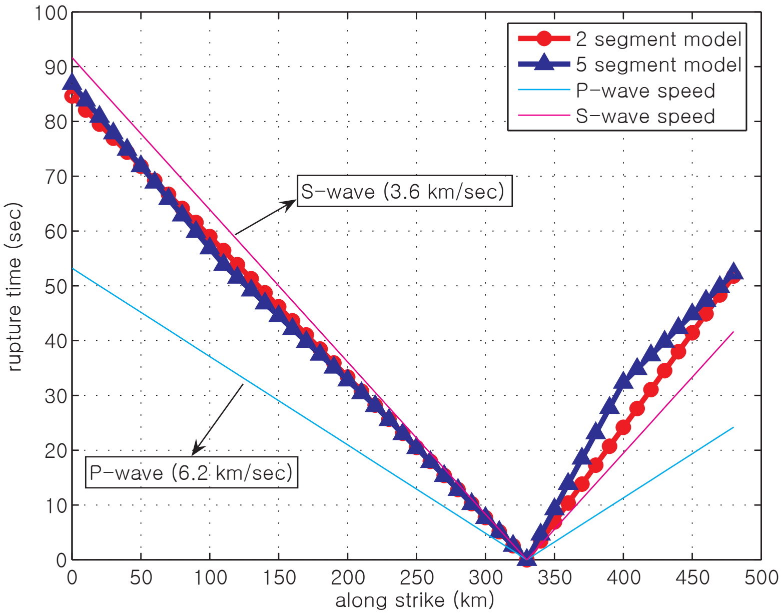

100
90
80
70
60
50
40
30
20
10
0
rupture time (sec)
0
50
100
150
200
250
300
350
400
450
500
along strike (km)
2 segment model
5 segment model
P−wave speed
S−wave speed
S−wave (3.6 km/sec)
P−wave (6.2 km/sec)

Figure 5

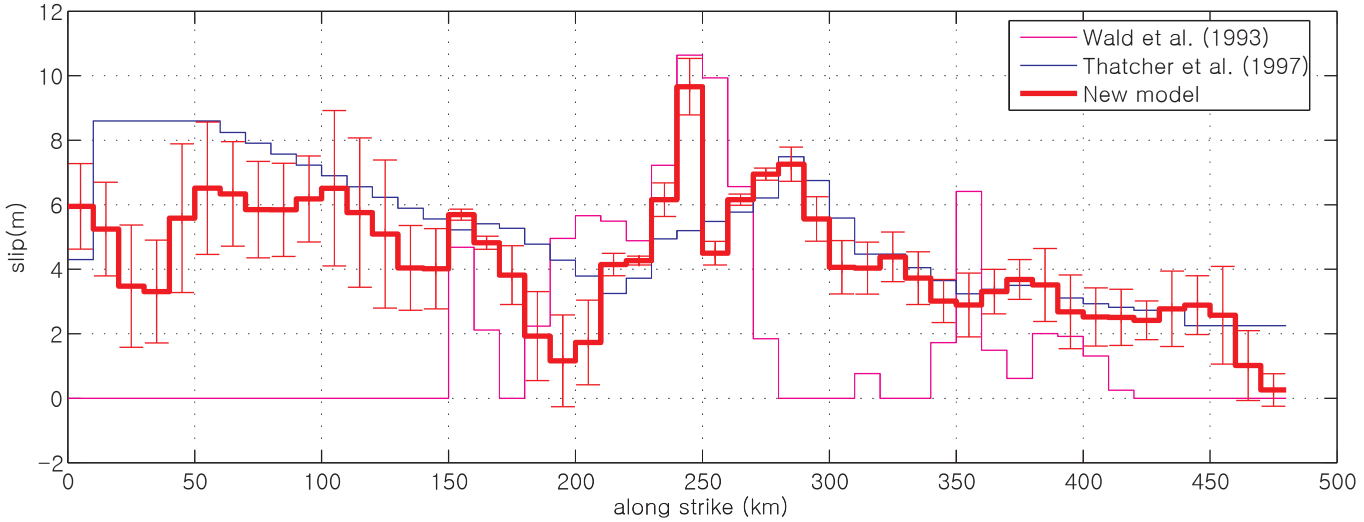

Cape Mendocino Point Arena Santa Rosa San Francisco San Juan Bautista

Figure 6

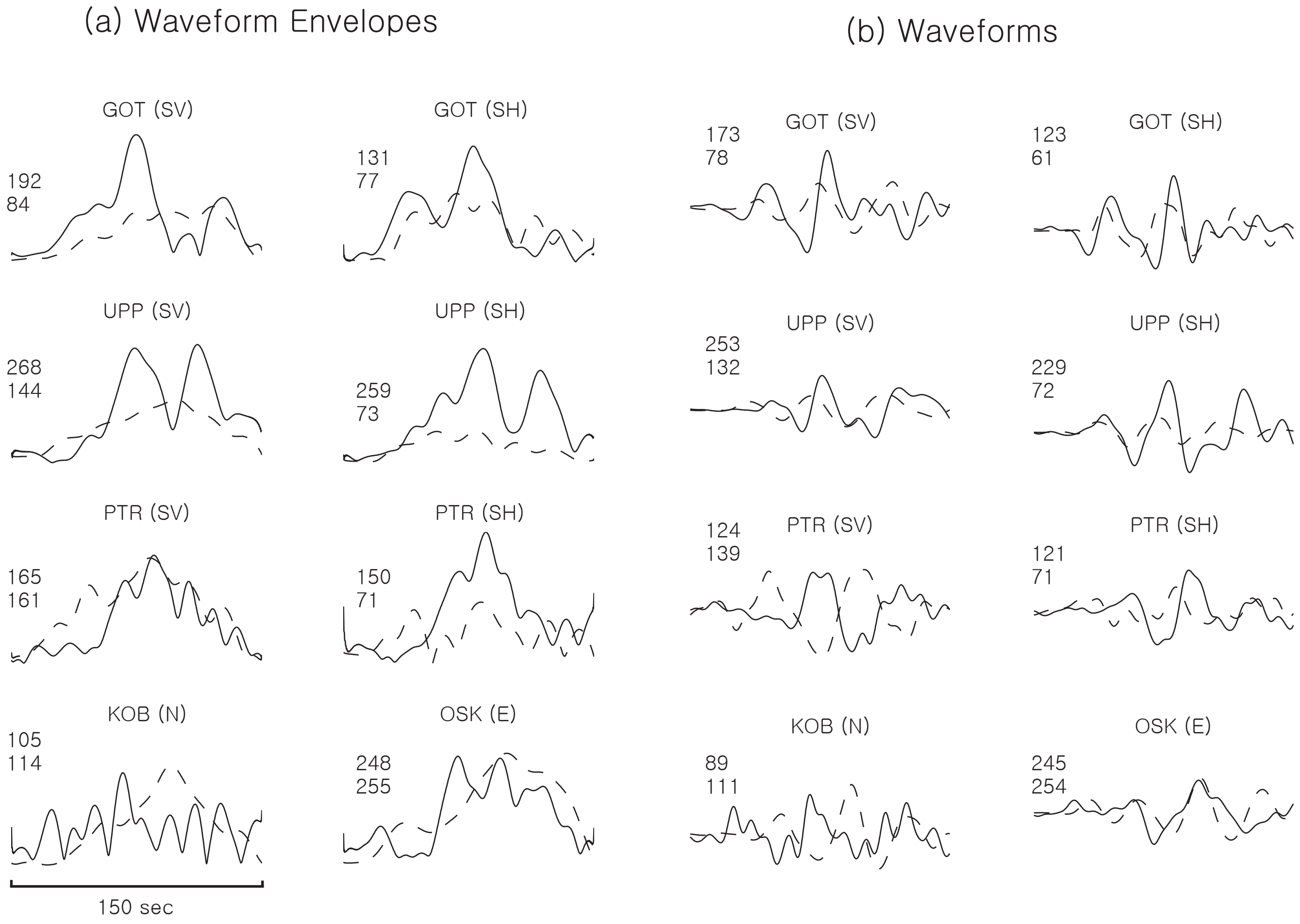
(a) Waveform Envelopes
(b) Waveforms
GOT (SV)
192
84
GOT (SH)
131
77
UPP (SV)
268
144
UPP (SH)
259
73
PTR (SV)
165
161
PTR (SH)
150
71
KOB (N)
105
114
OSK (E)
248
255
150 sec
GOT (SV)
173
78
GOT (SH)
123
61
UPP (SV)
253
132
UPP (SH)
229
72
PTR (SV)
124
139
PTR (SH)
121
71
KOB (N)
89
111
OSK (E)
245
254

Figure 7

(a) Apparent Source Time Function

(b) Stacked Apparent STF

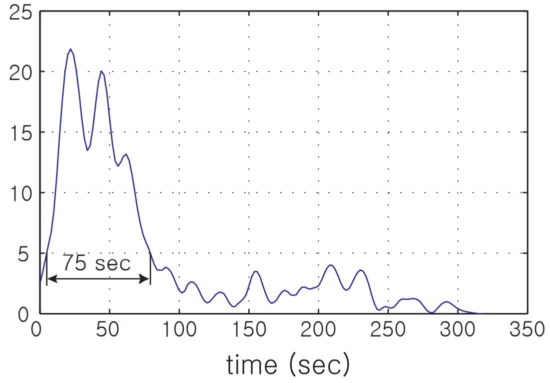

(c) Apparent Duration

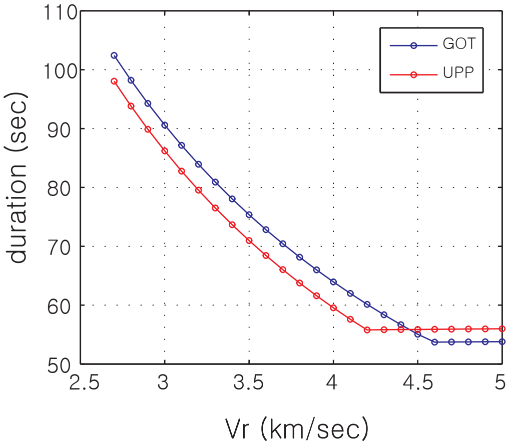

Figure 8